Dislocation Distribution, Crystallographic Texture Evolution, and Plastic Inhomogeneity of Inconel 718 Fabricated by Laser Powder Bed Fusion

Jalal Al-Lami,* Thibaut Dessolier, Samuel R. Rogers, Talha Pirzada, and Minh-Son Pham*

Plastic inhomogeneity, particularly localized strain, is one of the main mechanisms responsible for failures in engineering alloys. This work studies the spatial arrangement and distribution of microstructure (including dislocations and grains) and their influence in the plastic inhomogeneity of Inconel 718 fabricated by additive manufacturing (AM). The bidirectional scanning strategy with no interlayer rotation results in highly ordered alternating arrangements of coarse Goss-like {110}<001> textured grains separated by fine Cube-like {100}<001> textured grains. The bidirectional strategy also results in an overall high density of geometrically necessary dislocations (GNDs) that are particularly dense in the fine grains. Although the Cube-like texture desirable for isotropy is dominant, it gradually weakens during plastic deformation and the undesirable Goss-like component (second most dominant in the as-built microstructure) increases. The highly clustered and bimodal distribution of fine and coarse grains, textures, and GND densities causes fast localized roughening during deformation, particularly along the line row of fine Cube-like grains. However, the chessboard strategy results in a lower GND density and a comparatively more random distribution of crystallographic texture and GNDs, with a dominant Cube-like component (and much lower Goss-like texture) that remains stable throughout plastic deformation. This results in more uniform deformation, reducing plastic inhomogeneity.

1. Introduction

Additive manufacturing (AM) offers an unprecedented ability to manufacture components of complex geometry[1,2] while simultaneously tailoring the microstructure on the grain level.[3–8] Due to the layerwise nature of the process, the printing parameters can be altered at different locations within individual layers to enable a fine-scale spatial engineering of the microstructure and achieve desired mechanical properties at specific locations.[9] However, the reliability of metal AM components is still limited primarily by challenges in fabricating high-performance components.[10–12] While advances in processing techniques have improved the understanding of the formation of defects such as porosity and cracks, and ways to minimize the defect densities,[13–15] in-depth understanding of the fine microstructure remains insufficient. In particular, the spatial arrangement and distribution of dislocations, grains and detailed crystallographic texture, and how such fine microstructure affects the local plastic deformation spatially in AM components are still unclear. Obtaining such understanding is crucial because most damage initiates in localized deformed regions.

The influential role of the scanning strategy in tailoring the microstructure during AM processing was previously highlighted. Many studies demonstrated the impact of the scanning strategy on the grain microstructure such as the size, morphology, and overall crystallographic texture[4–6,8,16–23] and its influence on the global deformation behavior.[24–29] Altering the scanning strategy changes the local heat flux, cooling rate, and the ratio of thermal gradient (G) to solidification rate (R), hence controlling the mode and length scale of the solidification microstructure.[30,31] For example, it was demonstrated that the chessboard scanning strategy with 67° interlayer rotation can often interrupt the epitaxial columnar growth and crystallographic texture in AM components,[18] and both the columnar morphology and texture are influential in the deformation behavior, including the fracture response. Gokcekaya et al.[8] demonstrated that uniaxial loading parallel to columnar grains deflects crack tip openings and leads to an improvement in ductility in comparison to loading perpendicular to grain boundaries. Jin et al.[32] also reported that the crack behavior under fatigue loading is affected by the columnar grain orientation with respect to

J. Al-Lami, T. Dessolier, S. R. Rogers, M.-S. Pham
Department of Materials
Imperial College London
South Kensington, London SW7 2AZ, UK
E-mail: j.al-lami18@imperial.ac.uk; son.pham@imperial.ac.uk

T. Pirzada
Department of Materials
University of Oxford
Oxford OX1 3PH, UK

The ORCID identification number(s) for the author(s) of this article can be found under https://doi.org/10.1002/adem.202400524.

the load direction. The crystallographic texture is also an influential factor in the plastic deformation behavior spatially and globally. For example, if the random texture is excluded, the Cube {001}<100> texture component results in the least anisotropy, whereas the Goss {110}<001> component causes the most anisotropy.[33] While the dominant crystallographic orientations in as-built AM microstructure were previously reported,[18,22,34,35] there is scarce knowledge of the detailed texture components and their evolution during plastic deformation. Even if a desirable initial texture was created in the as-built condition, it might evolve under mechanical loading into a less desirable one. Therefore, it is important to understand how the texture evolves during plastic deformation.

Among all reported scanning strategies, the chessboard strategy with a 67° layer rotation is often used to fabricate components, and multiple studies reported that this strategy helps in improving mechanical properties. For example, the chessboard strategy was reported to result in lower residual stresses[24–26] and reduced anisotropy.[18,23] Such improvements are often attributed to grain microstructure such as the grain morphology and crystallographic texture. However, the dislocation density and spatial distribution are also influential in the internal stresses (hence residual stresses of type-II and type-III[36]) and plastic inhomogeneity (hence the anisotropy). Plastic inhomogeneity is often demonstrated by plastic localization, which is one of the main mechanisms causing the initiation of cracks. Nevertheless, the role of the scanning strategy in controlling the density and spatial distribution of dislocations, such as geometrically necessary dislocations (GNDs), has not been sufficiently studied. Developing a fundamental understanding of the effect of the scanning strategy on the dislocation alignment and distribution will help in obtaining a better understanding of how the local plastic deformation progresses. This understanding will enable the enhancement of the mechanical properties thanks to the ability of engineering the microstructure on a subgrain level via AM processing.

In this study, a detailed investigation of the spatial arrangement and distribution of microstructure, including grains, crystallographic texture components, and dislocation density and distribution in as-built conditions, was performed. Two commonly used scan strategies (bidirectional without layer rotation and chessboard with 67° layer rotation) were used to examine the effect of the scan strategy on the microstructure, in particular the texture and density and distribution of GNDs. In addition, in situ tensile testing coupled with detailed microstructural characterization was performed to obtain direct observations of links between the microstructure and plastic inhomogeneity. The in situ tests also provide new insights into the evolution of the microstructure with straining and its impact on the spatial deformation behavior. The study was focused on Inconel 718, which is widely used in the aerospace, nuclear, automotive, and power generation industries.[37–46]

2. Experimental Section

Inconel 718 cylinders of 16 mm diameter and 150 mm length were fabricated horizontally, **Figure 1**a, by laser powder bed fusion (L-PBF) using a Renishaw AM250 machine operating in pulsed wave form. The starting powder was acquired from H.C. Starck and had a spherical morphology and a nominal particle size distribution of 15–45 µm. All cylinders were printed with a laser power of 200 W, hatch spacing of 0.08 mm, point distance of 0.06 mm, and exposure time of 0.0001 s. However, the scanning strategy was varied to alter the microstructure. Individual cylinders were printed using a bidirectional strategy with 0° interlayer rotation or a chessboard strategy with 67° interlayer rotation, which are henceforth referred to as B0 and CB67, respectively. A schematic showing the scanning strategies is shown in **Figure 2**. The scanning bidirections in the B0 strategy were parallel to the longitudinal axis of the cylinder. The build layers in the CB67 strategy comprised islands of a 5 × 5 mm² size scanned in random order. Within the individual islands, the laser followed a bidirectional scanning pattern, and the islands were rotated at 90° with respect to each other. Samples for microscopy and in situ tensile testing, Figure 1b, were extracted by wire electrical discharge machining.

The samples were prepared by grinding with SiC paper in gradual steps using 800, 1200, 2000, and 4000 P-grades, followed by polishing in a 50% solution of oxide polishing suspension
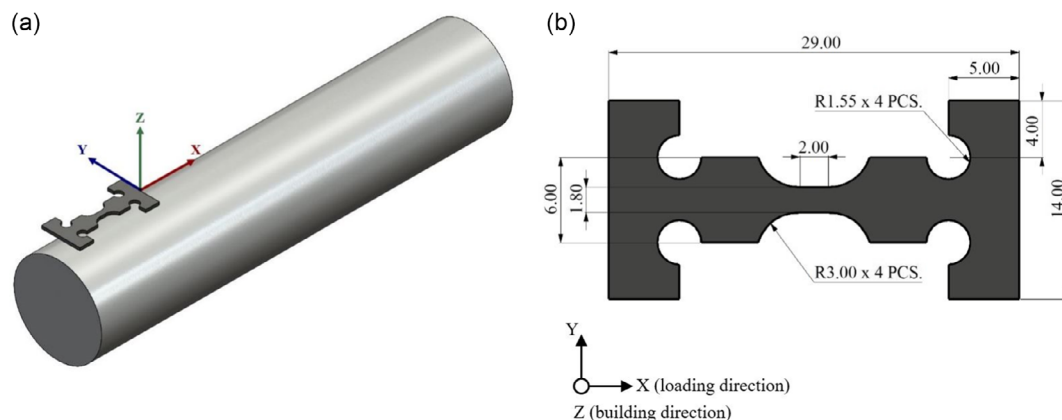

Figure 1. a) Model of the cylinders fabricated by L-PBF. An in situ tensile testing sample is depicted above, showing the test sample was machined along a cylinder fabricated horizontally using L-PBF. b) Dimensions of test samples. Note that the BD was along the Z axis, whereas the uniaxial LD was along X, which coincides with the scanning bidirections of the B0 strategy. All dimensions in mm and figures not to scale.
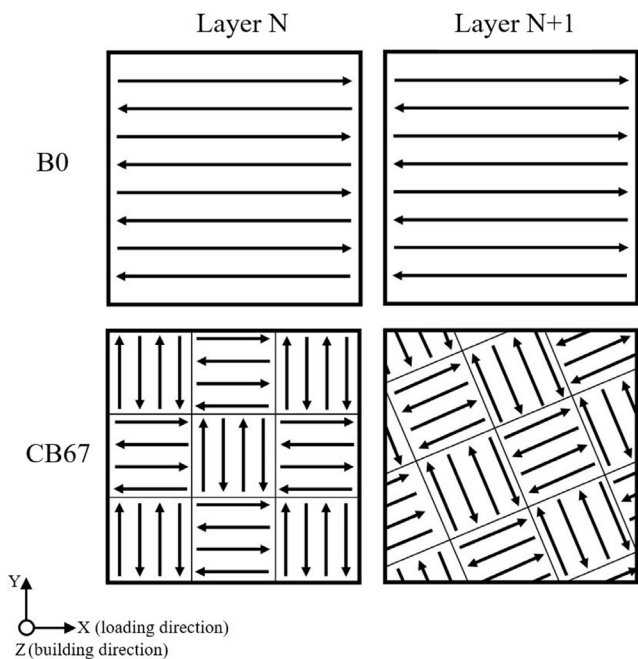
RIGHTSLINK

Figure 2. Schematic showing a top view (i.e., perpendicular to the BD Z) of the B0 and CB67 scanning strategies.

mixed with distilled water. To reveal the solidification microstructure, samples were etched with Aqua Regia (freshly mixed HCl with HNO_3 in a 3:1 ratio) for 8–10 s.

Microstructural characterization was performed using optical microscopy, scanning electron microscopy (SEM), electron backscatter diffraction (EBSD), and transmission electron microscopy (TEM). Secondary electron (SE) and backscatter electron (BSE) SEM imaging was performed using a voltage of 15 kV in a Zeiss Auriga microscope. Standard EBSD operating condition of 20 kV, 15 mm working distance, and 120 μm aperture was used, with a step size of 0.5 μm to capture the crystal orientation spread within the grains at small length scales. The EBSD data was analyzed using MTEX in MATLAB[47] and the grain reconstruction was performed using a grain boundary threshold of 5°. A JEOL JEM-2100F microscope operating at 200 kV was used to directly observe dislocations using TEM. Thin foils for TEM were prepared by twin-jet electropolishing in a Struers TenuPol-5. Electropolishing was performed at 20 kV and −5 °C in a solution of 10% perchloric acid in methanol. Because TEM is not effective in examining the dislocation distribution and density over a large area, EBSD was used to quantitatively characterize the dislocation condition (including density and distribution). It should be noted that EBSD is only able to quantify GNDs. However, it was found that GNDs colocated with the total dislocations in as-built alloys fabricated by AM.[32,48] Therefore, the spatial characterization of GNDs also provides insights into the spatial distribution of total dislocations. In this study, GNDs were measured from the EBSD data using MTEX.[47] The EBSD–GND density calculations were based on the measurement of the crystal orientation spread within individual grains. EBSD was used to quantify the variation in the crystallographic orientation between neighboring points to calculate the lattice curvature tensor and

dislocation density tensor.[49] The mathematical framework on which the MTEX code is based is provided in Pantleon's study.[50]

To study the evolution of the microstructure and its correlation with the deformation behavior, in situ tensile testing experiments using EBSD mapping and optical microscopy were performed separately. In EBSD in situ testing, the samples were held in a Gatan stage fitted inside an FEI Quanta FEG 650 SEM equipped with an EBSD system. EBSD scans were acquired on the undeformed samples and at strain levels of 4%, 7%, 10%, and after fracture, using the same EBSD operating condition listed previously but with a step size ranging from 1 to 2 μm. Uniaxial loading was performed on the samples with the loading direction (LD) being parallel to the scanning direction (SD) of the B0 strategy. The tests were performed at room temperature and at a strain rate of 10^{-3} per second. The evolution of near ideal Cube-like, Copper-like, S-like, Brasslike, and Goss-like texture components (**Table 1**) was examined and correlated with the deformation behavior. Analysis of texture components was performed using MTEX[51] and a 20° threshold was applied (i.e., grains within 20° of the orientation of interest were considered). Optical microscopy in situ tensile testing was performed by uniaxially loading the samples at the same strain rate of 10^{-3} per second in a Gatan stage fitted under an Olympus BX35M optical microscope. One micrograph was captured every second. To correlate the observations with the microstructure, ex situ EBSD maps of the region of interest in in situ optical microscopy tensile testing were acquired before and after deformation. In addition, surface topographical changes were measured on the deformed samples using a Zygo white light interferometer. In situ optical microscopy tensile testing helped to better reveal sites of intense roughening that cannot be clearly observed under the SEM. Additional tensile tests were performed on the B0 and CB67 conditions with digital image correlation (DIC) full-field strain measurements. In preparation for DIC testing, the samples were ground, polished, and sprayed with a white primer followed by black paint to create a speckle pattern. Testing was performed at the same strain rate of 10^{-3} per second in a Gatan stage placed under a camera capturing one image per second, and the images were processed in GOM Correlate software.

3. Results and Discussion

3.1. Role of Scan Strategy in Grain Microstructure and GND Distribution

The as-built microstructure of Inconel 718 processed by L-PBF is shown in **Figure 3**. In both the B0 and CB67 conditions, fine cells

Table 1. Texture components specified in Miller indices and Euler angle notation.

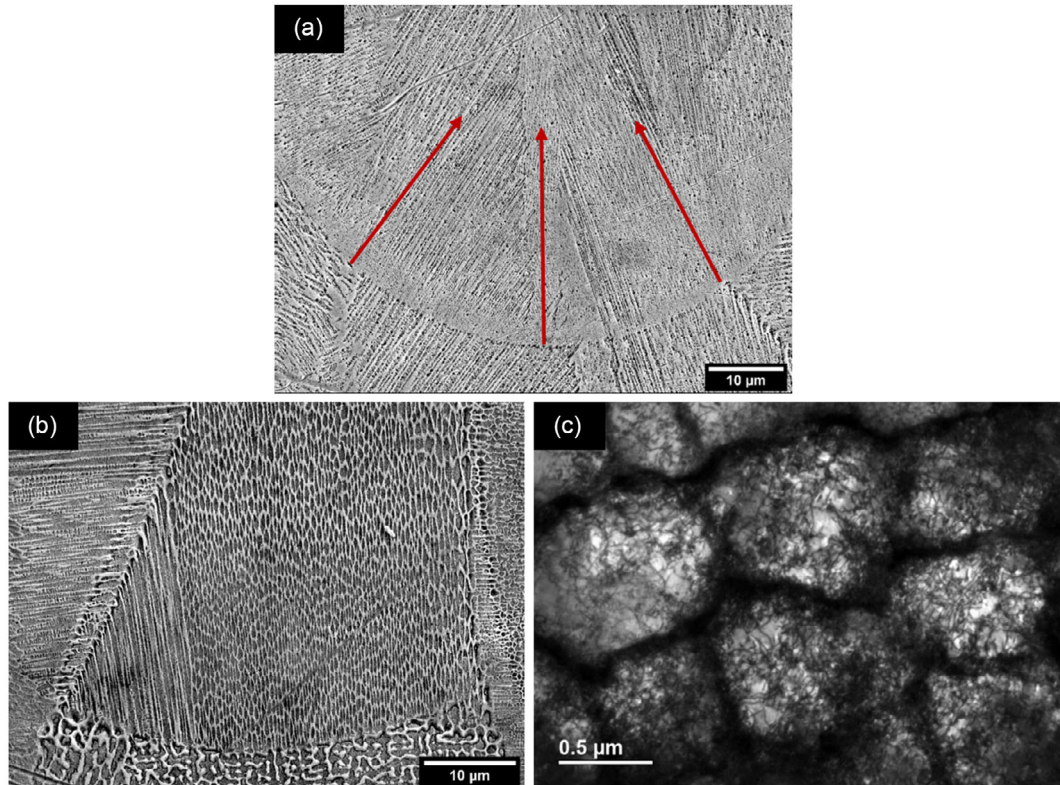| Texture component	Miller indices	Bunge $(\varphi_1, \theta, \varphi_2)$
Cube	$\{001\}\langle100\rangle$	(0, 0, 0)
Copper	$\{112\}\langle11\bar{1}\rangle$	(40, 65, 26)
S	$\{123\}\langle63\bar{4}\rangle$	(32, 58, 18)
Brass	$\{110\}\langle\bar{1}12\rangle$	(35, 45, 0)
Goss	$\{110\}\langle001\rangle$	(0, 45, 0)

Figure 3. As-built microstructure of Inconel 718 processed by L-PBF. a) Microstructure in a deposition bead with arrows showing the growth direction of cells that were initially almost perpendicular to the fusion boundary. b) Side-branching across the fusion boundary was seen in the top left region. c) Cellular dendrites containing a high density of dislocations, particularly at the boundaries. While the TEM foil was taken from a B0 sample, the observations are representative and applicable to the CB67 condition as well.

(or dendrites) can be seen growing in a direction nearly perpendicular to the melt pool fusion lines, as indicated by the arrows in Figure 3a. This growth direction is antiparallel to the maximum thermal gradient.[18] However, as the local thermal gradient changes with locations, in particular at the fusion boundary at which there are often changes of 90°, crystal cells (or dendrites) can still epitaxially grow by side-branching, Figure 3b. The same underlying mechanisms of crystal growth were observed in both the B0 and CB67 conditions. However, the scanning strategies induced different microstructure, particularly concerning the grain alignment and crystallographic texture, in agreement with previous reports.[5,18,22,52,53] The alignment of melt pools along the vertical building direction (BD) in the B0 strategy promotes the continuous epitaxial columnar growth of slender grains along the centerline of consecutive melt pools. On the sides of melt pools, the local changes in thermal gradient promote the epitaxial growth by side-branching with one of the $<001>$ orientations aligned at around 45° to the BD, making a $<101>$ orientation parallel to the BD. This results in a microstructure comprising thin and highly columnar grains of $<001>$ orientation (in the center of deposition beads/tracks) alternated by coarser grains of $<101>$ orientation at the sides, with respect to the BD, as shown in **Figure 4**a. Correspondingly, the view perpendicular to the BD of samples of the B0 strategy showed a highly ordered arrangement of coarse

grains of $<101>$ orientation separated by rows of fine grains of $<001>$ orientation, Figure 4b. The EBSD–inverse pole figures (IPF) with respect to the scanning bidirections (i.e., IPF-X) of the B0 condition showed a strong texture along the $<001>$ fiber, **Figure 5**. This is reflected in the pole figure, **Figure 6**a, which showed that $<001>$ was highly aligned to the scanning bidirections. The reason for this strong texture is because crystals grow along a $<001>$ that is antiparallel to the maximum heat flux that is the scan direction. Introducing rotation between deposition layers (e.g., by CB67 strategy) disrupts the thermal profile and interrupts the continuous epitaxial growth of cells along the melt pool's centerline observed in the B0 condition, resulting in less columnar grains, a wider grain size distribution, Figure 4e,f and 5b, and more random texture, namely, the $<001>$ along X (or Y) were much weakened in comparison with the B0, Figure 6a,b. The quantified average grain size along the BD in the B0 and CB67 conditions was 30 and 23 μm, respectively. We will show later in this study that the change in the scan strategy alters not only the arrangement, size, and distribution of grains, but also the dislocation density and spatial distribution.

The dendrite arm spacing in the B0 and CB67 conditions was measured to be 0.46 ± 0.04 and 0.56 ± 0.03 μm, respectively. Laves phase was observed in the interdendritic regions in both conditions. The coarser dendrite arm spacing induced by the CB67 scan strategy in this study is in alignment with other
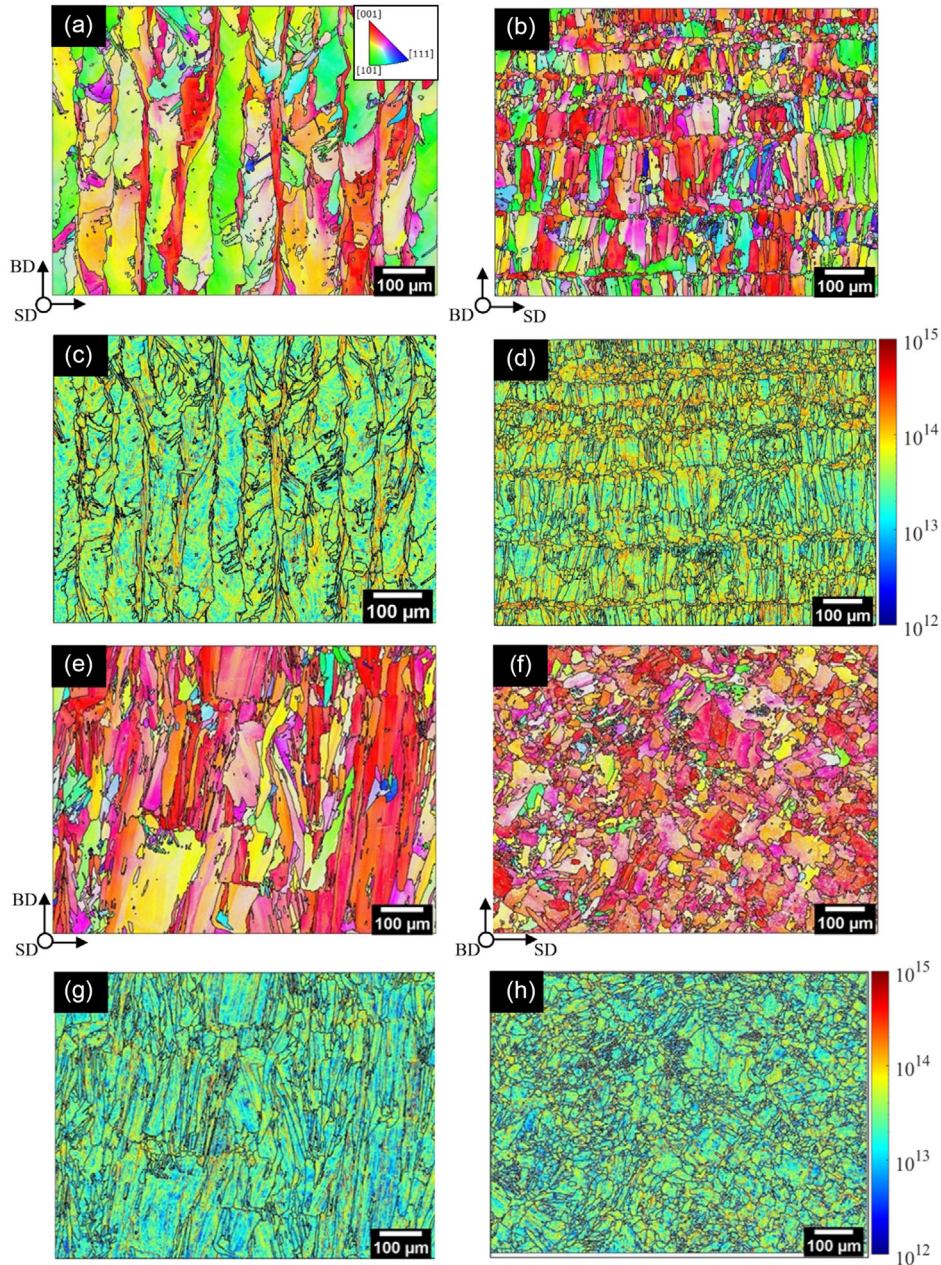
Figure 4. EBSD-IPF of the B0 and CB67 conditions with their corresponding GND spatial distribution maps, measured in m^{-2}. The B0 condition is presented in a–d), whereas the CB67 is presented in e–h). Note that the left column shows the cross section along the BD with IPF || BD, whereas the right column shows the top view along the SD with IPF || BD.

reports.[54,55] In comparison with the B0 strategy, the shorter scanning vectors inherent in the CB67 strategy result in less elapsed time between solidification and reheating of neighboring tracks (within the same scanning island), resulting in heat build-up that reduces the local thermal gradient and cooling rate. The slower cooling rate results in a coarser dendrite arm spacing and more pronounced chemical segregations, as detailed by some of the current coauthors in a separate study.[54] TEM examination revealed dense dislocations at the boundary of fine subgrain cellular dendrites, Figure 3c. Such solidification structures in as-built alloys were widely reported to be influential in strength and subsequently in the plastic deformation.[23,56–62]

The representative spatial distribution of GNDs in the B0 and CB67 conditions is presented in Figure 4c,d and g,h, respectively. The GNDs in the as-built condition are primarily located at and aligned along the boundaries of cells (or dendrites), as shown in **Figure 7**. This is in agreement with the TEM observation as it showed that most of dislocations were at cell boundaries (Figure 3c). Previous studies that examined dislocations by both TEM imaging and EBSD–GND analysis on the same sample
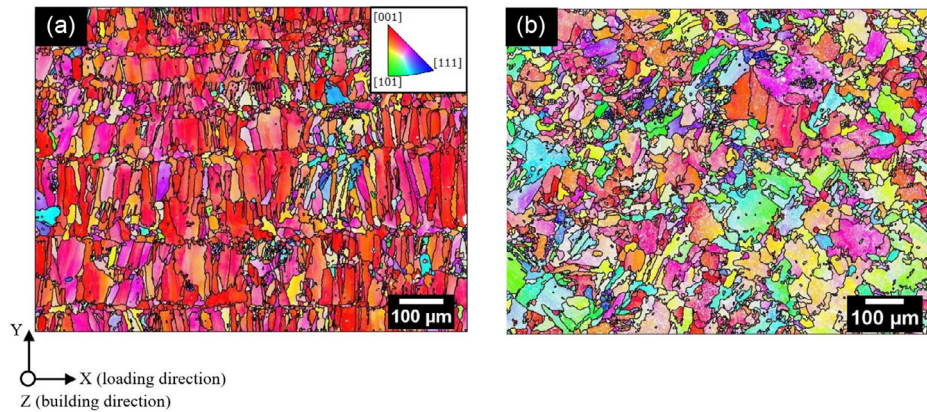
Figure 5. EBSD–IPF of the top view of the a) B0 and b) CB67 conditions. Note that IPF is with respect to the LD, not the BD as shown in Figure 4.
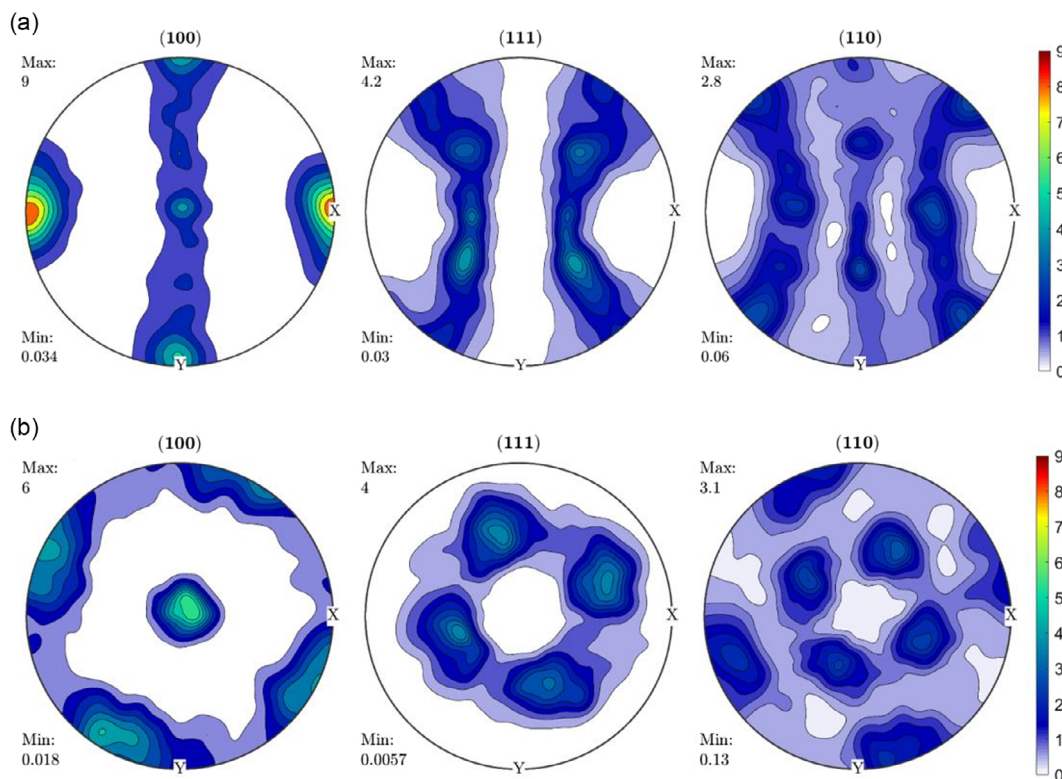

Figure 6. Pole figures of the a) B0 and b) CB67 conditions. Data acquired from the top-view maps.

confirmed the colocation of GNDs with statistically stored dislocations and their high density at cellular boundaries.[48] The measurement of GNDs using EBSD enables the correlation of the distribution of GND density with other microstructural features such as the grain size and orientation over areas larger than those captured by TEM.

The top-view GND map of the B0 condition (Figure 4d) shows that the GND alignment is nearly orthogonal to the SD as the cells' growth direction was perpendicular to the scan direction due to the fast laser beam speed. The GND accumulation was particularly very high in the fine grains of the $<001> \parallel$ BD

orientation (Figure 4c,d and g,h, and 8). In the B0 condition, the fine grains were along the centerline of deposition tracks (Figure 4c,d). The high GND density in the red $<001>$ elongated centerline grains is believed to have developed primarily because of two reasons. First, although the ordered stacking of melt pools promotes the continuous epitaxial growth (i.e., without side-branching) of the centerline grains, the stacking is not perfect in the process of layer-upon-layer deposition inherent in AM, resulting in a slight misalignment between consecutive layers. This essentially causes some variations in the heat flux along the centerline (hence thermal strain) between the vertical melt
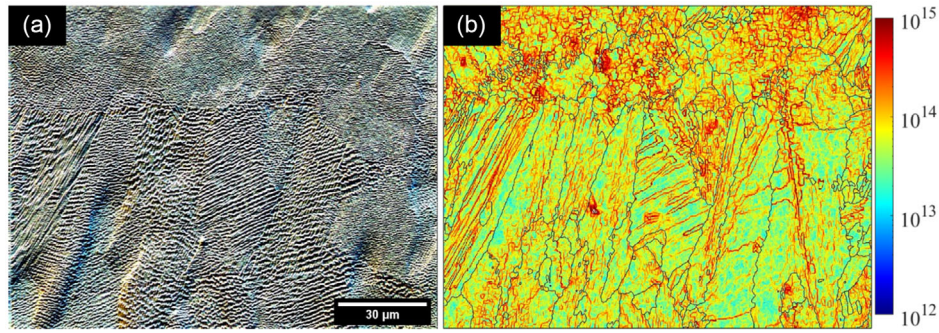
Figure 7. GNDs located at and aligned along the boundaries of cellular dendrites: a) SEM micrograph showing the cellular arrays in as-built Inconel 718; b) corresponding GND spatial distribution map, measured in m^{-2}. While the representative figures are from a B0 sample, the presented correlation between cell boundaries and GNDs is also applicable to the CB67 condition.
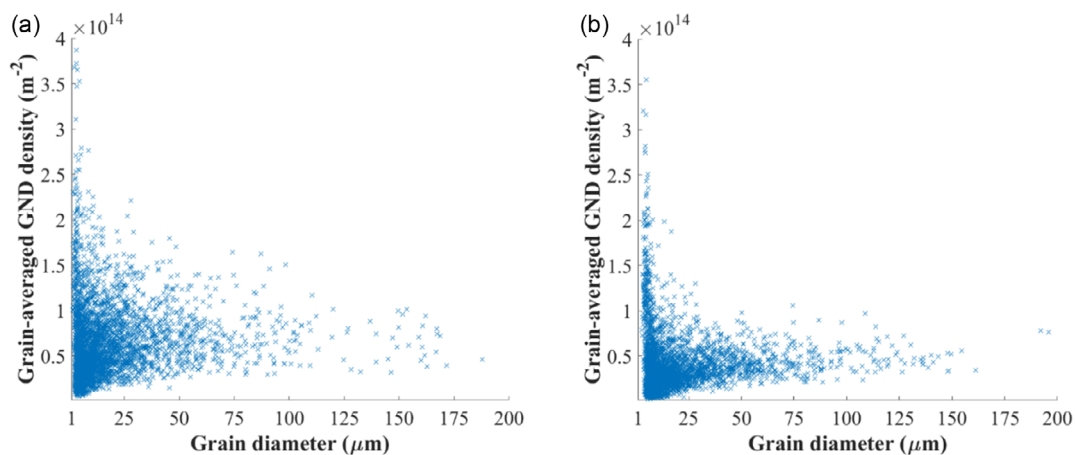

Figure 8. GND density as a function of grain diameter in the as-built and undeformed a) B0 condition and b) CB67 condition. The data was measured from the top-view maps.

pools in consecutive layers. If the variation is not large enough (found to be within about 30°[18]) to interrupt the continuous epitaxial growth, the existing centerline grains would continue growing vertically and dislocations need to be generated to accommodate the thermal strain induced by the variations. Second, the centerline grains are the last regions to solidify within a melt pool and their growth is constrained by the surrounding solids that shrink due to thermal contraction during cooling.[63,64] The surrounding contraction causes tension on the fine centerline grains,[65–67] which promotes the generation of dislocations in them.

The tensile properties of the B0 and CB67 are shown in **Figure 9**a and **Table 2**. The B0 strategy exhibited a higher strength consistent with what has been reported in literature[19,68,69] and this was previously attributed solely to the grain boundary strengthening effect imposed by the fine grains (Figure S1, Supporting Information). However, this study demonstrates that the strengthening effect is also due to the higher GND accumulation, particularly in the fine centerline grains induced by this scan strategy. The results also show that the change in scan strategy from B0 to CB67 significantly varied the GND spatial distribution, alignment, and density. In the

CB67 condition, dislocations were distributed more uniformly and their total density was much lower in comparison with the B0 condition, as shown in Figure 4 and 8. Indeed, the average GND density in the CB67 condition was 6.1×10^{13} m^{-2}, whereas it was 7.6×10^{13} m^{-2} in the B0 condition. The overall lower density of dislocations in the CB67 condition reduces the global residual stress. Also, the more uniform distribution of dislocations should be beneficial as it reduces the build-up of type-II and type-III residual stresses and the anisotropy in the builds. The reduction in anisotropy enabled by varying the scan strategy helps explain the more isotropic response reported in CB67 builds.[18] While the strains to failure of the two conditions were almost the same, it is worth noting that DIC tensile testing revealed that, immediately prior to failure, strain localization was more intense and encompassed a larger area of the gauge region in the B0 condition (Figure 9b) in comparison with the CB67 condition (Figure 9c).

3.2. Microstructure Evolution and Spatial Plastic Deformation

The previous section described the effect of the B0 and CB67 scanning strategies on the as-built microstructure (such as the
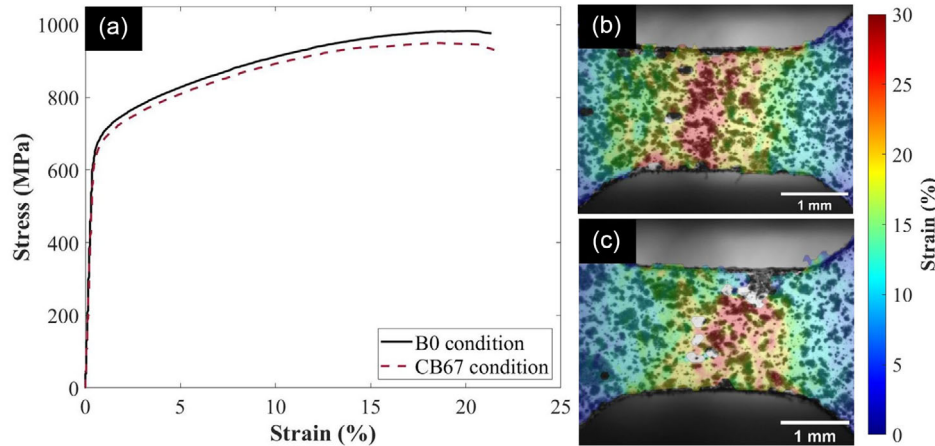
**ADVANCED
SCIENCE NEWS**

www.advancedsciencenews.com

**ADVANCED
ENGINEERING
MATERIALS**

www.aem-journal.com

Figure 9. a) Representative stress–strain curves of the B0 and CB67 conditions. The full-field strain distribution immediately prior to fracture in the b) B0 and c) CB67 conditions is presented. Strain localization appears to be comparatively more intense in the B0 condition.

Table 2. Tensile properties.

	Yield strength [MPa]	Ultimate tensile strength [MPa]	Total elongation [%]
B0 condition	672	982	21
CB67 condition	648	949	21

grain microstructure and the density and distribution of GNDs). In this section, the influence of the microstructure on the spatial deformation behavior is examined. In particular, Figure 9 suggests that the inhomogeneity of plasticity developed faster in the B0 than in CB67. Therefore, in situ mechanical testing in microscope was carried out to examine the development of local plasticity in the two build conditions.

In situ tensile testing under an optical microscope revealed the quick development of inhomogeneous topographical changes. For both the B0 and CB67 conditions, significant variation in surface topography was observed in the vicinity of boundaries between grains of significant crystallographic misorientation, for example, around the cluster of grains labeled "1" in **Figure 10**a,b. This surface roughening happened because of plastic strain incompatibility and restricted slip transmission across boundaries between neighboring grains of different crystallographic orientations. The difficulty of slip transmission across grain boundaries is governed by the misorientation between the two adjacent grains with respect to the LD and the type of grain boundary between them. While the <001> || LD grains were preferably oriented for easy octahedral (111)<110> slip, the <111> || LD grains were not favorably oriented. For slip system activation, <111> || LD grains should rotate to a more favorable orientation, but this rotation is resisted by the neighboring grains.[70] The difficulties in dislocation slip transmission from the <001> || LD grains to the <111> || LD grains resulted in intense surface topographical change in the vicinity of the grain cluster "1". This effect is seen for both scan strategy conditions and is further elaborated by another in situ tensile test in SEM/EBSD, **Figure 11**. For example, grains "1" and "2" had similar

orientations, resulting in good transmission of dislocations between the two grains, Figure 11a,b. However, slip lines were discontinued at the boundary between grains "2" and "3" as grain "3" had a different crystallographic orientation and was not preferably oriented for slip, as indicated by its high Taylor factor (Figure 11c), resulting in more obvious changes in surface topography between grains "2" and "3" in comparison with that between grains "1" and "2". In other words, Figure 10 and 11 exemplify that roughening (associated with plastic inhomogeneity) across the material is primarily governed by the underlying grain microstructure. Indeed, surface roughness examinations performed on the deformed samples showed that roughening is highly correlated with the spatial distribution of grains, Figure 10c,d. In particular, roughening was especially intensified along the line cluster of fine grains of a high dislocation density and a predominant texture of <001> || LD along the centerline of deposition tracks in the B0 condition, Figure 10c,d. The onset of plasticity is mainly influenced by 1) the critical resolved shear stress that depends on the dislocation density and 2) the applied shear stress resolved on a slip system that depends on the crystallographic orientation with respect to the LD, that is, the Schmid factor. The fine centerline grains in the B0 microstructure have a high critical resolved shear stress due to their high initial dislocation density. However, the centerline grains have <101>{111} well aligned with the LD to have high resolved shear stress for dislocation slip. Figure 10a,b shows that the fine grains plastically deformed more extensively in comparison to coarser grains that had lower initial densities of dislocations but were less aligned to the LD, leading to more surface roughening in regions of fine grains.

Figure 12 shows EBSD–IPF scans along the LD with the corresponding GND maps in the gauge region near the fracture surface. On average, the GND density substantially increased from the as-built and undeformed condition of the B0 (and CB67) samples, from 7.6×10^{13} m^{-2} (and 6.1×10^{13} m^{-2}) to 1.9×10^{14} m^{-2} (and 1.5×10^{14} m^{-2}) after fracture, respectively. Most notably, the GND accumulation increased within both the soft and most of hard grains, highlighting that the hard grains were eventually plastically deformed. The location of high GND accumulation
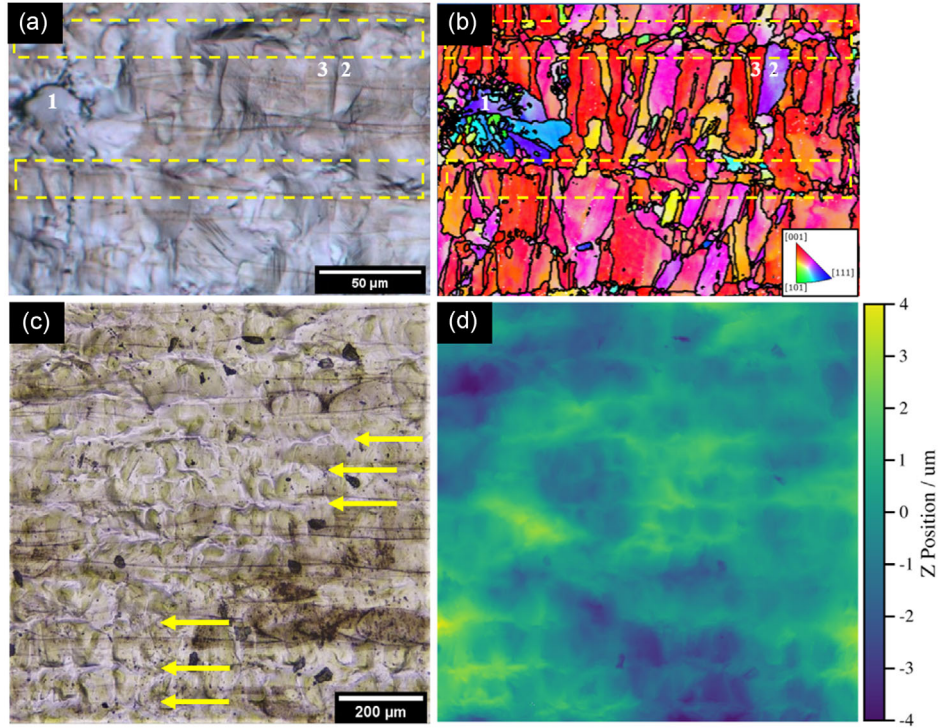
Figure 10. Effect of the underlying grain microstructure on the spatial deformation response. a) Optical micrograph of the deformed B0 condition, and b) its corresponding EBSD–IPF along the horizontal LD. Pronounced variation in surface topography is observed across boundaries between grains of significant crystallographic misorientation and along line clusters of fine <001> || LD grains, as indicated by the yellow rectangles. The direct observation of such correlation between roughening and the line clusters of fine grains in the B0 condition is further evident in c) the optical micrograph and d) corresponding surface topography map. The yellow arrows in (c) highlight locations of line clusters of fine grains.
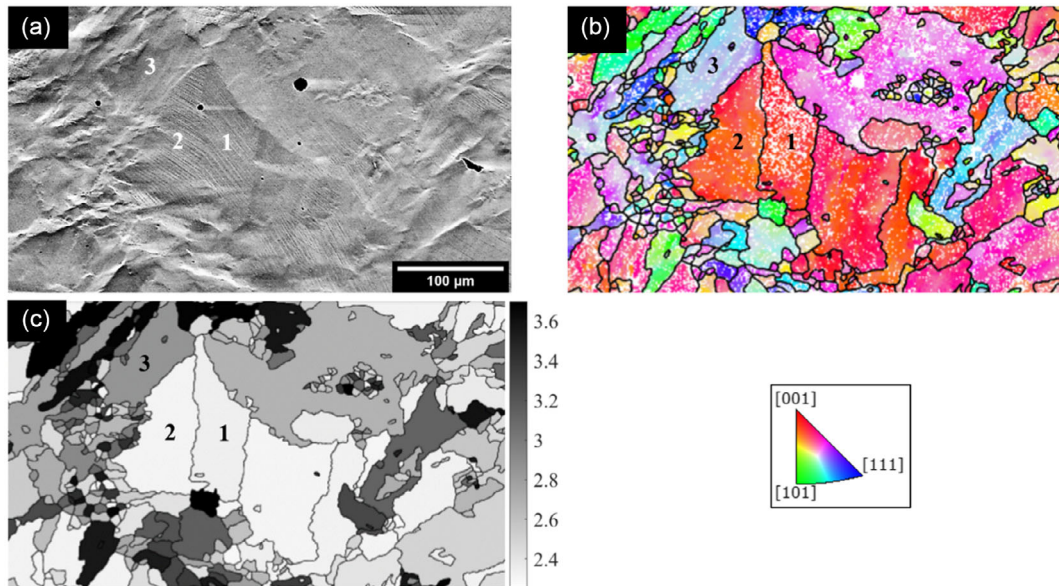

Figure 11. Slip transmission across neighboring grains in the CB67 condition at 10% strain. All figures are of the same region: a) SEM image; b) EBSD–IPF along the LD; c) Taylor factor map.

appeared to be along the cell boundaries, the same as it was before deformation. This suggests a significant role of the AM-inherent cellular structures in impeding and retaining

dislocations in AM-processed alloys, contributing to increasing the strength of the material and regulating the spatial plastic deformation. While in wrought alloys dislocation accumulation
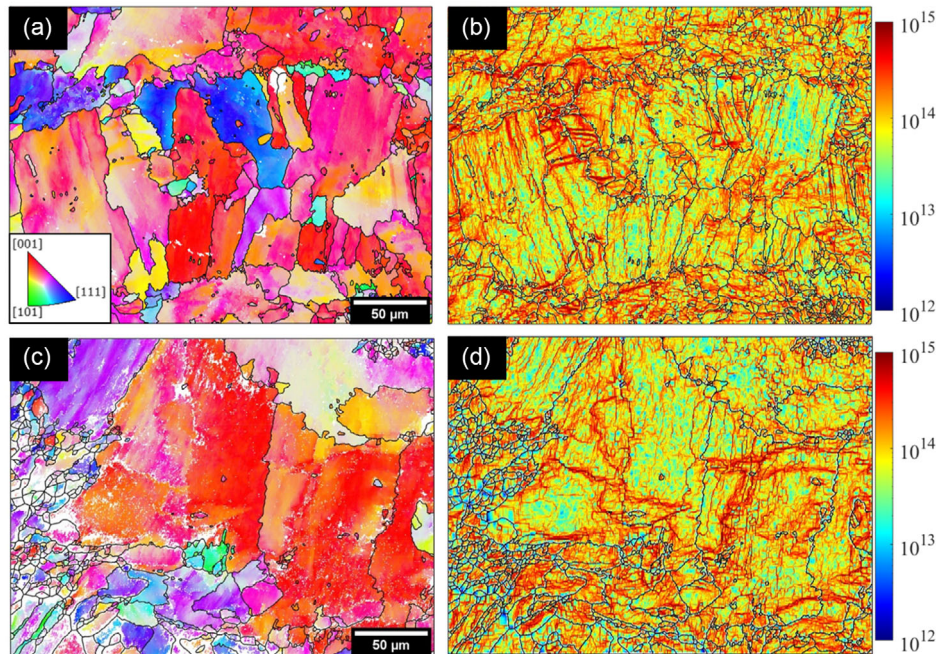
**ADVANCED
SCIENCE NEWS**
www.advancedsciencenews.com

**ADVANCED
ENGINEERING
MATERIALS**
www.aem-journal.com

Figure 12. EBSD–IPF along the horizontal LD with their corresponding GND maps, measured in m^{-2}, in the gauge region near the fracture surface: a,b) B0 condition; c,d) CB67 condition.

occurs most intensely near high-angle grain boundaries, in AM-processed alloys the boundaries of cellular structures within grains serve as additional effective obstacles to dislocation slip, hence accumulation sites of dislocations.[60,62]

3.3. Texture Evolution during Plastic Deformation

Crystallographic texture is an influential factor in the plastic deformation behavior spatially and globally.[71] AM alloys have been often reported to be strongly textured in the as-built condition. Therefore, it is necessary to study the evolution of texture components with strain. Main texture components such as Cube-like, Copper-like, S-like, Brass-like, and Goss-like components were quantified from the as-built (undeformed) condition to fracture for the B0 and CB67 samples, **Figure 13**. The undeformed B0 microstructure contained mostly Cube-like (35.8%) and Goss-like (27.0%) texture components. During the in situ tensile test, the Cube-like and Goss-like components in the B0 microstructure most rotated at the lower strain range. For example, after a nominal strain of 4%, the Cube-like texture component weakened by 3.1% while the Goss-like component increased by 2.7%. Such changes were more significant than those of other texture components such as Copper-like (decrease by 0.4%), S-like (increase by 2.0%), and Brass-like (increase by 1.4%), Figure 13a. The Cube orientations belong to the soft <001> fiber and have a low Taylor factor (and similar for the Goss orientations if the loading is parallel to a <001>), whereas the Copper and Brass on the <111> fiber are not preferably oriented for plasticity and are more resistant to deformation and grain rotation (hence texture changes), as discussed in section 3.2. The stability of the Brass component in Ni-based superalloys

is in agreement with previous studies.[70,72,73] Figure 13b reveals that at the point of fracture, the Cube-like texture decayed while the Goss-like and Brass-like components intensified in the B0 condition.

Figure 13c shows that the Cube-like texture component was also the most dominant in the as-built CB67 condition, but lower than in the initial B0 condition. Also, contrary to the B0, the Goss-like component was comparatively much lower in the initial CB67 condition. While the Cube-like and Goss-like components showed minimal change throughout the deformation of the CB67 (Figure 13d), the Copper-like, S-like, and Brass-like components reorientated and most notably changed at strain levels exceeding 10%, with the Copper-like component intensifying the most and increasing by 6.9% by the point of fracture. The difference in the grain reorientation behavior is governed by both the initial crystallographic orientations of the individual grains and the neighboring grains. The crystallographic orientation changes because of elastic lattice distortion and grain rotation associated with dislocation slip under loading and boundary condition constraints.[74]

It has been well demonstrated that the Goss texture component causes the most plastic anisotropy in components, whereas the Cube component results in the least anisotropy (apart from the totally random texture), in particular in multiaxial deformation.[33,71] This present study shows that the as-built B0 condition contained a higher fraction of the preferable Cube-like texture component in comparison with the CB67 condition. However, the Cube-like component degraded quickly with plastic deformation in the B0 condition, but the Goss-like texture component, which was initially also high in the as-built B0 condition, increased during loading. The decrease in Cube-like and the
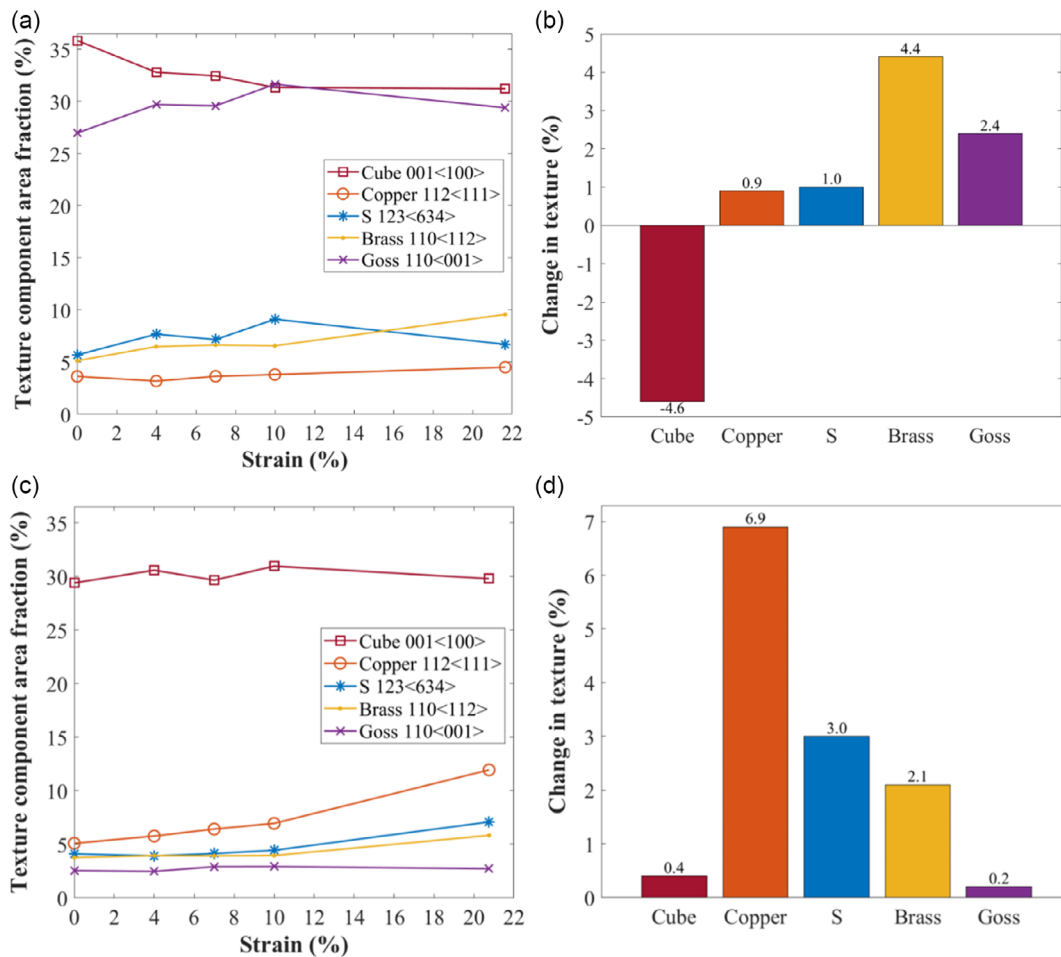
Figure 13. Evolution of texture component area fraction across the strain intervals and their overall change from the as-built to fractured: a,b) B0 condition and c,d) CB67 condition.

increase in Goss-like components in the B0 condition during deformation could intensify the plastic anisotropy. On the contrary, the dominant Cube-like texture and the substantially lower fraction of the Goss-like component remained stable throughout the plastic deformation of the CB67 condition, helping to maintain a homogeneous deformation behavior. Our previous study shows that plastic inhomogeneity can result in early crack initiation.[40]

3.4. Impact of Scanning Strategy on Plastic Inhomogeneity

Plastic inhomogeneity in AM alloys is governed by the arrangement, morphology, size distribution, and crystallographic texture of grains and the spatial distribution of dislocations. The results presented in section 3.1 and 3.3 demonstrate that such microstructure can be effectively controlled by the laser scanning strategy, thereby influencing the spatial plastic deformation. The B0 strategy creates elongated columnar grains of alternating <001> and <101> orientations with respect to the BD (Figure 4a). The top view perpendicular to the BD of the B0 condition showed highly ordered alternating rows of fine grains of Cube-like <001> orientations (containing a very high dislocation density,

including GNDs) and coarse grains of Goss-like <101> orientations (with a lower density of GNDs that are aligned perpendicular to the scan direction, Figure 4b,d. In essence, the B0 strategy creates segregated zones of grains of two dominant textures with bimodal size distribution and dislocations. Such segregated distributions cause significantly inhomogeneous plastic deformation, hence surface roughness. This is exemplified by localized surface roughening along the line row of fine grains in the B0 condition, Figure 10. In contrast, the island scanning and interlayer rotation in the CB67 strategy interrupt the epitaxial columnar growth and result in comparatively more random grain morphologies, crystallographic orientations, and GND distributions (Figure 4e,f). The more random grain microstructure and absence of line cluster of fine grains in the CB67 minimize the plastic inhomogeneity in this condition. The faster development of plastic localization in B0 would result in lower elongation in comparison to CB67. However, the strains to failure of the two scan strategies were similar (Figure 9a). This was attributed to the presence of porosity. In addition, although the preferred Cube-like texture component area fraction was shown to be the most dominant component in both the B0 and CB67 conditions, the CB67 contained a much lower fraction of the

Goss-like component, which is the most anisotropic component.[33] The Cube-like and Goss-like texture components were found to remain stable throughout the plastic deformation of the CB67 condition (Figure 13c,d), which is expected to help retain the plastic homogeneity and minimize localization upon further plastic straining – this is desirable for AM builds.

4. Conclusion

This work investigates spatial aspects of key microstructure such as the grain arrangement, dislocation condition (density and distribution), and crystallographic texture (namely Cube-like, Goss-like, Copper-like, Brass-like, and S-like components) and their effects on the plastic deformation inhomogeneity in Inconel 718 fabricated by L-PBF with varied scan strategies. The bidirectional strategy without layer rotation (i.e., B0) resulted in a highly ordered arrangement of coarse grains separated by line clusters of fine grains along the center of deposition tracks. The fine grains contained a much higher density of dislocations, in particular GNDs, than the coarse grains. The GND alignment in the coarse grains was polarized and primarily orthogonal to the laser scanning direction. The fine grains were found to have strong Cube-like texture (which induces good isotropy) while the coarse grains were of strong Goss-like texture (which often causes severe anisotropy). Under uniaxial tension, the Cube-like texture component was weakened while the Goss-like component was strengthened. Such microstructure arrangement and distribution promoted plastic inhomogeneity in the B0 condition. It was found that roughening was highly correlated with plastic localization associated with the grain distribution. In particular, roughening was most apparent along the line cluster of fine grains and across grain boundaries between grains of Cube-like texture and Goss-like texture. Such microstructure is characteristic of the B0 scan strategy. As plastic strain localization is a main mechanism responsible for crack initiation, such microstructure is unfavorable for high-performance builds made by AM. Despite the higher tensile strength induced by the B0 scan strategy, its inhomogeneous plastic deformation behavior would make it not ideal. In contrast, the microstructure created by the chessboard strategy with 67° layer rotation (i.e., CB67) was much more favorable. In particular, texture and dislocation distribution were much more random, dislocation density was lower, and the orderly alternating arrangement of coarse/fine grains found in the B0 condition was eliminated. The CB67 strategy also resulted in a strong Cube-like texture component, but much weaker Goss-like component. The Cube-like component was stable during plastic deformation, making it much more favorable for homogeneous deformation.

Supporting Information

Supporting Information is available from the Wiley Online Library or from the author.

Acknowledgements

Conflict of Interest

The authors declare no conflict of interest.

Data Availability Statement

The data that support the findings of this study are available from the corresponding author upon reasonable request.

Keywords

[1] M.-S. Pham, C. Liu, I. Todd, J. Lertthanasarn, *Nature* **2019**, *565*, 305.
[2] K. Liu, R. Sun, C. Daraio, *Science* **2022**, *981*, 975.
[3] N. Raghavan, S. Simunovic, R. Dehoff, A. Plotkowski, J. Turner, M. Kirka, S. Babu, *Acta Mater.* **2017**, *140*, 375.
[4] R. R. Dehoff, M. Kirka, W. J. Sames, H. Bilheux, A. S. Tremsin, L. E. Lowe, S. S. Babu, *Mater. Sci. Technol.* **2015**, *31*, 931.
[5] K. A. Sofinowski, S. Raman, X. Wang, B. Gaskey, M. Seita, *Addit. Manuf.* **2021**, *38*, 101809.
[6] K. Sofinowski, M. Wittwer, M. Seita, *Addit. Manuf.* **2022**, *52*, 102683.
[7] S. Gao, Z. Li, S. Van Petegem, J. Ge, S. Goel, J. V. Vas, V. Luzin, Z. Hu, H. L. Seet, D. F. Sanchez, H. Van Swygenhoven, H. Gao, M. Seita, *Nat. Commun.* **2023**, *14*, 6752.
[8] O. Gokcekaya, T. Ishimoto, S. Hibino, J. Yasutomi, T. Narushima, T. Nakano, *Acta Mater.* **2021**, *212*, 116876.
[9] V. A. Popovich, E. V. Borisov, A. A. Popovich, V. S. Sufiiarov, D. V. Masaylo, L. Alzina, *Mater. Des.* **2017**, *114*, 441.
[10] D. D. Gu, W. Meiners, K. Wissenbach, R. Poprawe, *Int. Mater. Rev.* **2012**, *57*, 133.
[11] J. J. Lewandowski, M. Seifi, *Annu. Rev. Mater. Res.* **2016**, *46*, 151.
[12] T. DebRoy, H. L. Wei, J. S. Zuback, T. Mukherjee, J. W. Elmer, J. O. Milewski, A. M. Beese, A. Wilson-Heid, A. De, W. Zhang, *Prog. Mater. Sci.* **2018**, *92*, 112.
[13] A. A. Martin, N. P. Calta, S. A. Khairallah, J. Wang, P. J. Depond, A. Y. Fong, V. Thampy, G. M. Guss, A. M. Kiss, K. H. Stone, C. J. Tassone, J. Nelson Weker, M. F. Toney, T. van Buuren, M. J. Matthews, *Nat. Commun.* **2019**, *10*, 1987.
[14] C. Panwisawas, B. Perumal, R. M. Ward, N. Turner, R. P. Turner, J. W. Brooks, H. C. Basoalto, *Acta Mater.* **2017**, *126*, 251.
[15] C. L. A. Leung, S. Marussi, R. C. Atwood, M. Towrie, P. J. Withers, P. D. Lee, *Nat. Commun.* **2018**, *9*, 1355.
[16] T. Ishimoto, K. Hagihara, K. Hisamoto, S. H. Sun, T. Nakano, *Scr. Mater.* **2017**, *132*, 34.
[17] H. L. Wei, J. Mazumder, *Sci. Rep.* **2015**, *5*, 16446.
[18] M.-S. Pham, B. Dovgyy, P. A. Hooper, C. M. Gourlay, A. Piglione, *Nat. Commun.* **2020**, *11*, 749.
[19] S. Tekumalla, C. J. Eng, A. T. S. Wei, K. Manickavasagam, M. Seita, *Addit. Manuf.* **2022**, *59*, 103111.
[20] G. P. Dinda, A. K. Dasgupta, J. Mazumder, *Scr. Mater.* **2012**, *67*, 503.

[21] L. N. Carter, C. Martin, P. J. Withers, M. M. Attallah, *J. Alloys Compd.* **2014**, *615*, 338.

[22] A. Piglione, B. Dovgyy, C. Liu, C. M. Gourlay, P. A. Hooper, M. S. Pham, *Mater. Lett.* **2018**, *224*, 22.

[23] B. Dovgyy, A. Piglione, P. A. Hooper, M. S. Pham, *Mater. Des.* **2020**, *194*, 108845.

[24] S. Goel, M. Neikter, J. Capek, E. Polatidis, M. H. Colliander, S. Joshi, R. Pederson, *Mater. Des.* **2020**, *195*, 109045.

[25] M. F. Zaeh, G. Branner, *Prod. Eng.* **2010**, *4*, 35.

[26] J. P. Kruth, L. Froyen, J. Van Vaerenbergh, P. Mercelis, M. Rombouts, B. Lauwers, *J. Mater. Process. Technol.* **2004**, *149*, 616.

[27] H. Ali, H. Ghadbeigi, K. Mumtaz, *Mater. Sci. Eng., A* **2018**, *712*, 175.

[28] J. Robinson, I. Ashton, P. Fox, E. Jones, C. Sutcli, *Addit. Manuf.* **2018**, *23*, 13.

[29] L. Parry, I. A. Ashcroft, R. D. Wildman, *Addit. Manuf.* **2016**, *12*, 1.

[30] M. Gäumann, C. Bezencon, P. Canalis, W. Kurz, *Acta Mater.* **2001**, *49*, 1051.

[31] J. C. Lippold, *Welding Metallurgy and Weldability*, John Wiley & Sons, New Jersey, USA **2014**.

[32] M. Jin, A. Piglione, B. Dovgyy, E. Hosseini, P. A. Hooper, S. R. Holdsworth, M. S. Pham, *Addit. Manuf.* **2020**, *36*, 101584.

[33] M. S. Pham, A. Creuziger, M. Iadicola, A. D. Rollett, *J. Mech. Phys. Solids* **2017**, *99*, 50.

[34] A. Tabei, E. Mirkoohi, H. Garmestani, S. Liang, *Int. J. Adv. Manuf. Technol.* **2019**, *103*, 1057.

[35] O. Zinovieva, A. Zinoviev, V. Romanova, R. Balokhonov, *Addit. Manuf.* **2020**, *36*, 101521.

[36] P. J. Withers, H. K. D. H. Bhadeshia, *Mater. Sci. Technol.* **2001**, *17*, 355.

[37] E. Hosseini, V. A. Popovich, *Addit. Manuf.* **2019**, *30*, 100877.

[38] R. E. Schafrik, D. D. Ward, J. R. Groh, *Proc. Int. Symp. Superalloys Var. Deriv.* **2001**, *1*, 1.

[39] B. Blakey-Milner, P. Gradl, G. Snedden, M. Brooks, J. Pitot, E. Lopez, M. Leary, F. Berto, *Mater. Des.* **2021**, *209*, 110008.

[40] J. Al-Lami, P. Hoang, C. Davies, T. Pirzada, M.-S. Pham, *Mater. Charact.* **2023**, *199*, 112815.

[41] R. C. Reed, *The Superalloys: Fundamentals and Applications*, Cambridge University Press, Cambridge, UK **2006**.

[42] D. Texier, J. Milanese, M. Jullien, J. Genée, J.-C. Passieux, D. Bardel, E. Andrieu, M. Legros, J.-C. Stinville, *Acta Mater.* **2024**, *268*, 119759.

[43] S. Sanchez, P. Smith, Z. Xu, G. Gaspard, C. J. Hyde, W. W. Wits, I. A. Ashcroft, H. Chen, A. T. Clare, *Int. J. Mach. Tools Manuf.* **2021**, *165*, 103729.

[44] L. Chechik, I. Todd, *Addit. Manuf. Lett.* **2023**, *6*, 100145.

[45] J. D. Pérez-Ruiz, L. N. L. de Lacalle, G. Urbikain, O. Pereira, S. Martínez, J. Bris, *Int. J. Mach. Tools Manuf.* **2021**, *170*, 103801.

[46] J. D. Pérez-Ruiz, F. Marin, S. Martínez, A. Lamikiz, G. Urbikain, L. N. López de Lacalle, *Mech. Syst. Signal Process.* **2022**, *168*, 108675.

[47] R. Hielscher, H. Schaeben, *J. Appl. Crystallogr.* **2008**, *41*, 1024.

[48] Y. S. J. Yoo, T. A. Book, M. D. Sangid, J. Kacher, *Mater. Sci. Eng., A* **2018**, *724*, 444.

[49] S. Birosca, G. Liu, R. Ding, J. Jiang, T. Simm, C. Deen, M. Whittaker, *Int. J. Plast.* **2019**, *118*, 252.

[50] W. Pantleon, *Scr. Mater.* **2008**, *58*, 994.

[51] G. Rafailov, E. N. Caspi, R. Hielscher, E. Tiferet, R. Schneck, S. C. Vogel, *J. Appl. Crystallogr.* **2020**, *53*, 540.

[52] J. J. Marattukalam, D. Karlsson, V. Pacheco, P. Beran, U. Wiklund, U. Jansson, B. Hjörvarsson, M. Sahlberg, *Mater. Des.* **2020**, *193*, 108852.

[53] S.-H. Sun, T. Ishimoto, K. Hagihara, Y. Tsutsumi, T. Hanawa, T. Nakano, *Scr. Mater.* **2019**, *159*, 89.

[54] V. Vieira, A. Piglione, M. Pham, S. Primig, *Addit. Manuf.* **2022**, *50*, 102540.

[55] A. Piglione, B. Attard, V. Vieira, C. S. Maldonado, M. M. Attallah, S. Primig, M. Pham, *Addit. Manuf.* **2021**, *47*, 102347.

[56] T. G. Gallmeyer, S. Moorthy, B. B. Kappes, M. J. Mills, B. Amin-Ahmadi, A. P. Stebner, *Addit. Manuf.* **2020**, *31*, 100977.

[57] M. E. Aydinöz, F. Brenne, M. Schaper, C. Schaak, W. Tillmann, J. Nellesen, T. Niendorf, *Mater. Sci. Eng., A* **2016**, *669*, 246.

[58] D. Zhang, W. Niu, X. Cao, Z. Liu, *Mater. Sci. Eng., A* **2015**, *644*, 32.

[59] M. Jin, E. Hosseini, S. R. Holdsworth, M.-S. Pham, *Addit. Manuf.* **2022**, *51*, 102600.

[60] Y. M. Wang, T. Voisin, J. T. McKeown, J. Ye, N. P. Calta, Z. Li, Z. Zeng, Y. Zhang, W. Chen, T. T. Roehling, R. T. Ott, M. K. Santala, P. J. Depond, M. J. Matthews, A. V. Hamza, T. Zhu, *Nat. Mater.* **2018**, *17*, 63.

[61] X. Wang, L. N. Carter, B. Pang, M. M. Attallah, M. H. Loretto, *Acta Mater.* **2017**, *128*, 87.

[62] L. Liu, Q. Ding, Y. Zhong, J. Zou, J. Wu, Y. L. Chiu, J. Li, Z. Zhang, Q. Yu, Z. Shen, *Mater. Today* **2018**, *21*, 354.

[63] O. Hunziker, D. Dye, R. C. Reed, *Acta Mater.* **2000**, *48*, 4191.

[64] N. Coniglio, C. E. Cross, *Int. Mater. Rev.* **2013**, *58*, 375.

[65] J. Liu, P. Zeng, Y. Wu, S. Kou, *Sci. Technol. Weld. Joining* **2020**, *25*, 431.

[66] S. Kou, *Acta Mater.* **2015**, *88*, 366.

[67] M. Rappaz, J. M. Drezet, M. Gremaud, *Metall. Mater. Trans. A* **1999**, *30A*, 449.

[68] H. Y. Wan, Z. J. Zhou, C. P. Li, G. F. Chen, G. P. Zhang, *Mater. Sci. Eng., A* **2019**, *753*, 42.

[69] A. Leicht, C. H. Yu, V. Luzin, U. Klement, E. Hryha, *Mater. Charact.* **2020**, *163*, 2.

[70] S. Birosca, F. Di Gioacchino, S. Stekovic, M. Hardy, *Acta Mater.* **2014**, *74*, 110.

[71] U. F. Kocks, C. N. Tomé, H.-R. Wenk, *Texture and Anisotropy: Preferred Orientations in Polycrystals and their Effect on Materials Properties*, Cambridge University Press, Cambridge, UK **1998**.

[72] J. Parkin, S. Birosca, *J. Alloys Compd.* **2021**, *865*, 158548.

[73] D. Raabe, Z. Zhao, S. J. Park, F. Roters, *Acta Mater.* **2002**, *50*, 421.

[74] A. Cottrell, *Dislocations and Plastic Flow in Crystals*, Clarendon Press, Oxford, UK **1953**.